J Appl Electrochem (2010) 40:1941–1947
DOI 10.1007/s10800-010-0170-2

ORIGINAL PAPER

A kinetic study on the electrodeposition of nickel nanostructure and its electrocatalytic activity for hydrogen evolution reaction

Morteza Torabi · A. Dolati

Received: 11 August 2009 / Accepted: 4 July 2010 / Published online: 14 July 2010

Abstract The electrodeposition of nickel was studied using electrochemical techniques in different electrolytes and various agents. The voltammetry analysis clearly showed that the electrodeposition of nickel was a diffusion-controlled process associated with a typical nucleation process. The current transients represented instantaneous nucleation with a typical three-dimensional (3D) growth mechanism. Scharifker's equations were derived for instantaneous and progressive nucleation of the 3D growth of the spherical centers under diffusion-controlled condition. The number of nucleation sites increased with the increment in overpotential and Ni^{2+} concentration. Atomic force microscopy was used to confirm the presumed model. Also, the electrocatalytic activities of the Ni films were investigated for hydrogen evolution reaction (HER). The electrocatalytic activity of the Ni nanostructure was three times higher than the 2D Ni microstructure when the overpotential of −1.2 V was applied. The HER current density at −1.4 V for Ni nanostructure (−20 mA cm^{-2}) was considerable with respect to the Ni microstructure (−8.46 mA cm^{-2}) too.

Keywords Nickel · Nanostructure · Thin film · Kinetic · Electrocatalytic activity

1 Introduction

Nanostructured materials consist of nanometer-sized particles and structures with lateral dimensions of less than 100 nm. Among various techniques for production of nanostructured materials, electrodeposition is technologically feasible and economically superior [1–3], because it has yielded (1) a number of nanometals [4–6] including Ni, Co, Cu, Ni–P, Ni–Mn, Ni–Zn, Ni– Fe, and Cu–Ni–P as well as compositionally modulated alloys (CMA) [7], laminated nanostructured metals [7], and nanomatrix composites such as Ni–SiC [8]; (2) products with various sizes and shapes [1, 2], e.g., powders, thin films, thick films, bulk materials and net-shaped and complex-shaped articles and (3) porosity-free finished products with very narrow grain size distribution [3]. These products, showing the exclusive attributes of high strength and ductility [5, 9], attract researchers to work on them for theoretical [10] or practical purposes [1–3]. Also, with other advantages such as low cost, low initial capital investment, high production rates, and technologically easy transfer from laboratory to existing infrastructure in electroplating industries, the electrochemical techniques brought about the first industrial application of nanomaterials.

On the other hand, producing energy from hydrogen is very attractive since it can resolve the exhaustion of fossil fuels and their environmental problems. In addition, hydrogen plays an important role in many applications, such as fuel cells [11]. Numerous studies have also been developed for hydrogen generation from water by electrolysis [12]. At present, water electrolysis is the sole commercialized technique to produce hydrogen.

Nickel and its alloys and compounds attract researchers due to their good electrocatalytic activity for hydrogen evolution reaction (HER), corrosive resistance to the strongly alkaline environment, and their low prices [13–15]. Furthermore, chemical and physical properties of electrodeposited nickel are strongly influenced by the deposition parameters.

M. Torabi (✉) · A. Dolati
Materials Science and Engineering Department,
Sharif University of Technology, P.O. Box 11365-9466,
Tehran, Iran
e-mail: torabi_morteza@yahoo.com

In this study, electrochemical techniques were employed to provide a better understanding of the cathodic behavior of the nickel deposition. The effects of complexing compounds on kinetics and surface morphology of the Ni electrodeposition were investigated. Moreover, electrocatalytic activities of the nickel micro- and nanostructures were examined for HER.

2 Experimental

All electrochemical experiments were performed using a three-electrode cell. A copper wire and a platinum plate (with 1 cm^2 area) were used as working and counter electrodes, respectively. Electrochemical potentials were recorded versus an Ag/AgCl reference electrode. The solutions were prepared by dissolving reagent grade chemicals (Merck, Germany) and double-distilled water. The working electrolytes were obtained by addition of solutions containing boric acid, sodium potassium tartarate, nickel sulfate, sodium saccharin, and cumarine as shown in Table 1. The solutions were adjusted to pH 5.5 ± 0.1 with suitable additions of H_2SO_4 or NaOH. All investigations were conducted at room temperature (25 °C).

The electrochemical experiments were controlled using an EG&G PAR potentiostat model 273A and software model M271. The voltammetry sweeps were recorded as a function of scan rate from 5 to 200 mV s^{-1}. The voltammetric scans were performed in the potential range from −0.1 to −1.7 V versus Ag/AgCl. The potentiostatic *I–t* transients were recorded at time intervals of 10 s. Also, HER activities have been studied by voltammetric scans at 5 mV s^{-1} in the negative direction at room temperature.

Topographic images of the deposits were also obtained by atomic force microscopy (AFM). These experiments were carried out in the ambient condition using Veeco CP Research instrument using Si cantilever.

3 Results and discussion

Voltammetry was utilized to obtain the potential regions and characterization of nickel electrodeposition. Figure 1a shows the typical irreversible voltammograms for deposition of nickel from sol. 1 (without boric acid). A broad cathodic peak is observed in the voltammogram at scan rate 5 mV s^{-1}, while no cathodic peak can be seen at higher scan rates. Readsorption of the reaction products may give rise to some complications at very low scan rates [16]. Indeed, sweeping with scan rate of 5 mV s^{-1} led to readsorption of the reaction product and consequently, raising a peak in the voltammogram.

If the ratio of the sodium potassium tartarate concentration (M) to nickel ion concentration (M) was about 1–1.5, the tartarate would deal as a complexing agent. Therefore, it would be expected that the system was governed by mass transport. Migration of the complexes to the electrode surface is more difficult than the solvated ion, and the reduction peak would arise in the voltammogram. On the other hand, if the ratio was less than 0.1, then the organic agent would deal as a surfactant and finer deposits would be expected.

In the sol. 1, the above ratio was about 0.35 that is between these two ranges and could be a surfactant or complexing agent. If the sodium potassium tartarate acted as a complexing additive, then the voltammograms would include a cathodic peak at higher scan rates. Therefore, the sodium potassium tartarate deals as a finer or surfactant during nickel electrodeposition. So, readsorption of the reaction products led to the cathodic peak at scan rate 5 mV s^{-1}.

Figure 1b shows the effect of the boric acid on the electrodeposition of the nickel from sol. 2. The scan rate was increased to avoid the problems of products readsorption. No diffusion peak was ,observed and electrodeposition of Ni in sol. 2 was charge-transfer-controlled. The voltammetry results (Fig. 1c) in the absence of the boric acid and sodium potassium tartarate (sol. 3) also show similar behavior to sol. 2.

Figure 2 shows voltammetry sweeps for different Ni^{2+} concentrations (12.09–69.92 g L^{-1}) in the presence of boric acid and sodium potassium tartarate (sol. 4). Increasing the nickel concentration shifted the nickel reduction peaks to more negative potentials with higher current contribution. It also reveals that nickel electrodeposition was purely diffusion-controlled at lower nickel concentrations in sol. 4.

Voltammograms in Fig. 3 are shown for different scan rates from 5 to 200 mV s^{-1} in sol. 4 with a constant nickel concentration (57.52 g L^{-1}). The nickel reduction peaks

Table 1 Composition of the electrolytes used in this study

Sol.	Boric acid (g L^{-1})	Sodium Potassium tartrate (g L^{-1})	Nickel sulfate (g L^{-1})	Sodium Saccharine (g L^{-1})	Cumarine (g L^{-1})
1	–	19.747	52.57	0.73	0.99
2	19.78	–	52.57	0.73	0.99
3	–	–	52.57	0.73	0.99
4	19.78	19.747	12.09–69.92	0.73	0.99

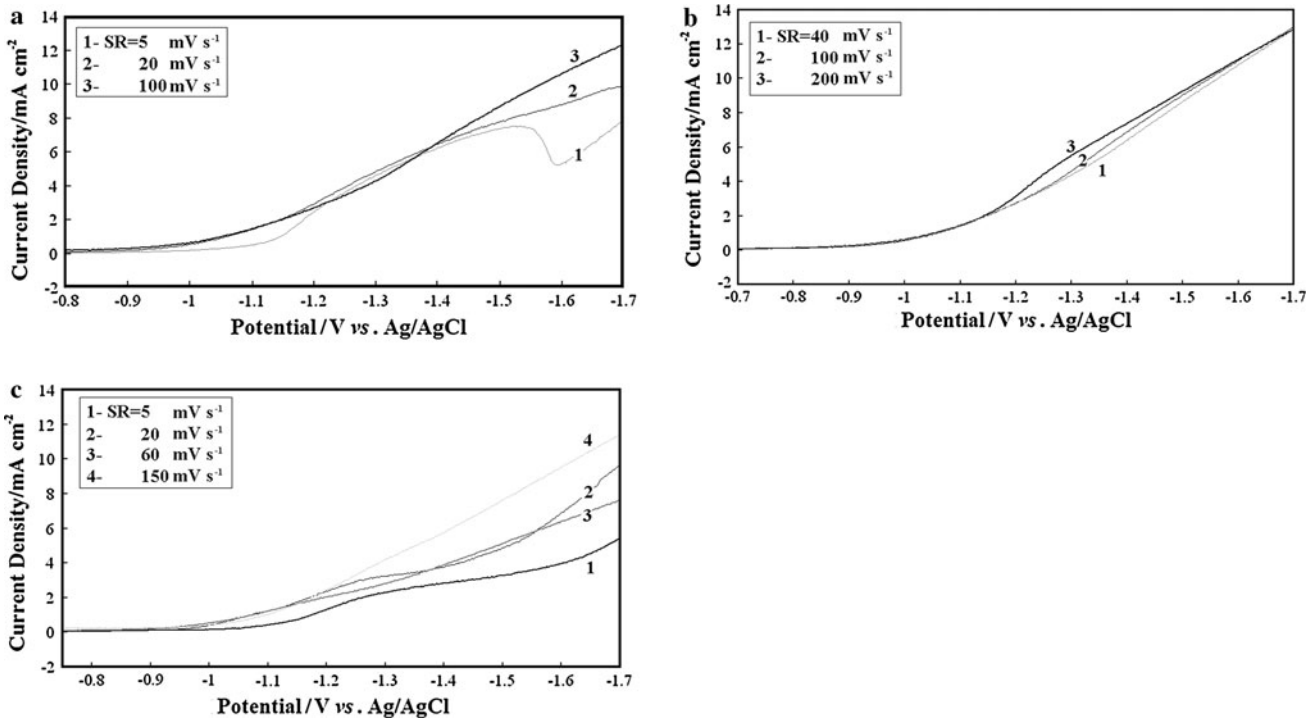

Fig. 1 Voltammograms for deposition of Nickel from, **a** sol. 1, **b** sol. 2, and **c** sol. 3

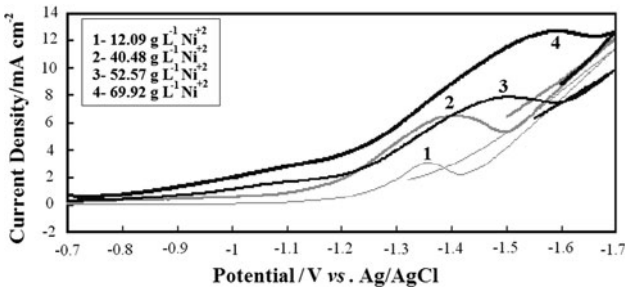

Fig. 2 Voltammograms for the Ni deposition in sol. 4, Ni^{2+} concentration from 12.096 to 69.92 g L^{-1} and $v = 20$ mV s^{-1}

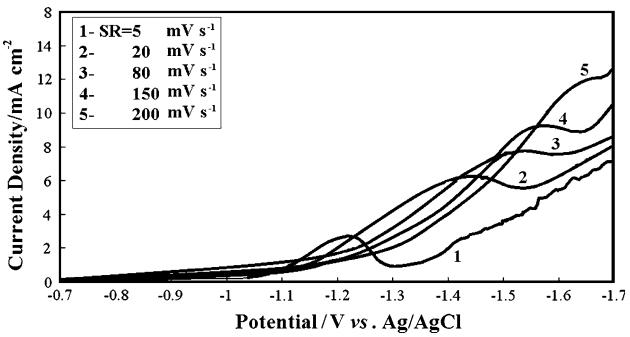

Fig. 3 Voltammograms for the Ni deposition in sol. 4, $[Ni^{2+}] = 57.52$ g L^{-1} and $v = 5$–200 mV s^{-1}

shifted to more negative potentials as well as higher current contribution, with increasing scan rates. The current density was increased with starting hydrogen reduction at the same time. All voltammograms also show a single kinetic peak according to the mass transfer process. Moreover, a current crossover on the cathodic branches indicates a typical nucleation process.

Delahay equations were applied to calculate the kinetic parameters such as αn_α, D, and the k_s. With regard to the Eq. 1 the αn_α could be derived.

$$E_p - E_{p/2} = -1.857\left(\frac{RT}{\alpha n_\alpha F}\right) \quad (1)$$

The linear proportion (Fig. 4a) of the current densities of the peaks versus the square root of the scan rates (I_p–$v^{1/2}$) implies that the process is diffusion-controlled. Therefore, the diffusion coefficients could be calculated from the slope of these lines by means of Eq. 2:

$$i_p = -0.496nFC_0^\infty\left(\frac{\alpha n_\alpha F}{RT}\right)^{1/2} D^{1/2}v^{1/2} \quad (2)$$

The k_s constant also is derived from Eq. 3. From the y-intercept of the E_p versus log(v) curves (Fig. 4b), the diffusion coefficients of nickel could be obtained as well.

$$E_p = K - \frac{2.3RT}{2\alpha n_\alpha F}\log v \quad (3)$$

The calculated parameters for different nickel concentrations are presented in Table 2. At higher nickel concentration there was a decrease and increase in αn_α and D, respectively. Moreover, increasing the cation

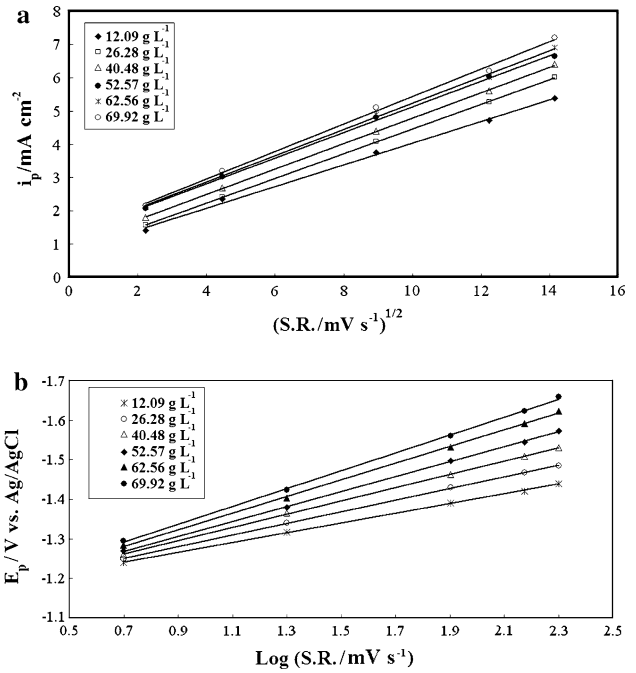

Fig. 4 **a** The I_p–$v^{1/2}$ curves for deposition of Ni in sol. 4, Ni^{2+} concentration from 12.096 to 69.92 g L^{-1}, **b** The E_p–log(v) curves for deposition of Ni in sol. 4, Ni^{2+} concentration from 12.096 to 69.92 g L^{-1}

Table 2 The kinetic parameters of nickel deposition

[Ni^{2+}] (g L^{-1})	αn_α	D ($\times 10^{-7}$, cm^2 s^{-1})	k_s ($\times 10^{-4}$)
12.09	0.525	3.7	1.9
26.28	0.521	3.85	2.1
40.48	0.517	4.1	2.4
52.57	0.514	4.5	3.7
62.56	0.512	4.8	4.3
69.92	0.505	5.3	5.6

concentration led to the enhancement of the solubility coefficient as well.

Chronoamperometric analysis was used to characterize the mechanism of nickel electrodeposition. Potentiostatic current transient curves for nickel electrodeposition from sol. 4 are shown in Fig. 5 at a wide range of the negative potentials from −1.1 to −1.4 V. More negative potentials than the equilibrium potentials were considered to study the Ni overpotential deposition (OPD). For nickel reduction at potentials more positive than −800 mV, only the double-layer capacitance was recorded, and no pronounced nucleation behavior was observed. Each transient in Fig. 5a has one well-defined recognizable current maximum as a clear first peak followed by a sharp fall and posterior growth. These *I–t* transients have a normal dependence to overpotential. The critical time for nucleation was decreased with shifting the potential to more

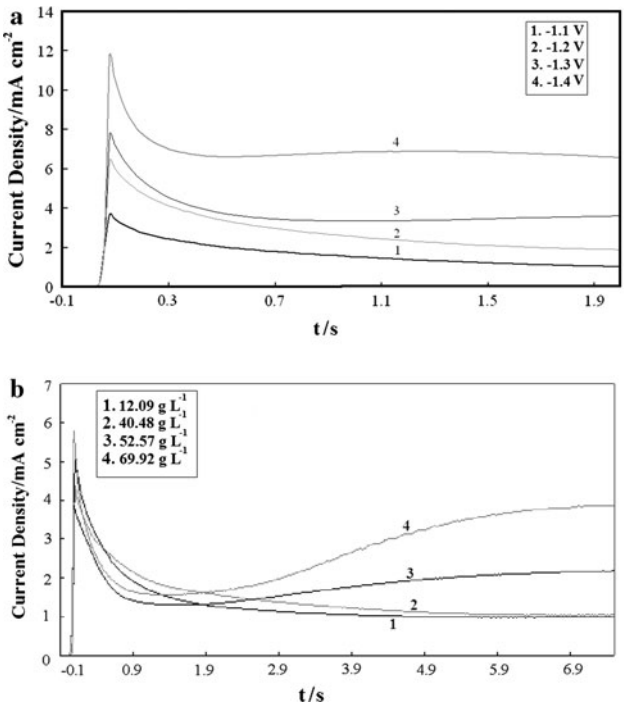

Fig. 5 Potentiostatic *I–t* transients for deposition of the Ni in sol. 4, **a** Ni^{2+} concentration = 57.52 g L^{-1}, potential range from −1.1 to −1.4 V versus Ag/AgCl and **b** Ni^{2+} concentration from 12.096 to 69.92 g L^{-1} and potential = −1.2 V versus Ag/AgCl

negative values. The particular shapes of the *I–t* transients clearly show that the nucleation and growth process is embodied in the electrodeposition of nickel and diffusion is a rate-limiting process. However, the current transients are best described according to the following equations for the metal forming solutions [17, 18]:

$$I(t) = \frac{nAFD^{1/2}C^{\infty}}{\pi^{1/2}t^{1/2}}[1 - \exp(-N_0\pi kDt)], \quad (4)$$

$$\text{where } k = (8\pi C^{\infty}M/\rho)^{1/2}$$

$$\text{At long time, } I(t) = \frac{nAFD^{1/2}C^{\infty}}{\pi^{1/2}t^{1/2}} \quad (5)$$

where, the A is the area of the electrode, D is the diffusion coefficient, C^{∞} is the bulk concentration of the Ni^{2+}, M is the molar mass, ρ is the density of the Ni, and N_0 is the number of the nucleation sites.

Each transient in Fig. 5b has one well-defined recognizable current maximum followed by a sharp fall and posterior growth as same as Fig. 5a. The curves have a normal dependence to nickel concentration.

Linear behavior of I versus $t^{1/2}$ plot (Fig. 6a) at the rising portion of the transients confirms the previous results in which mass transfer governs the system kinetics. The slope and intercept of the lines are depended to the

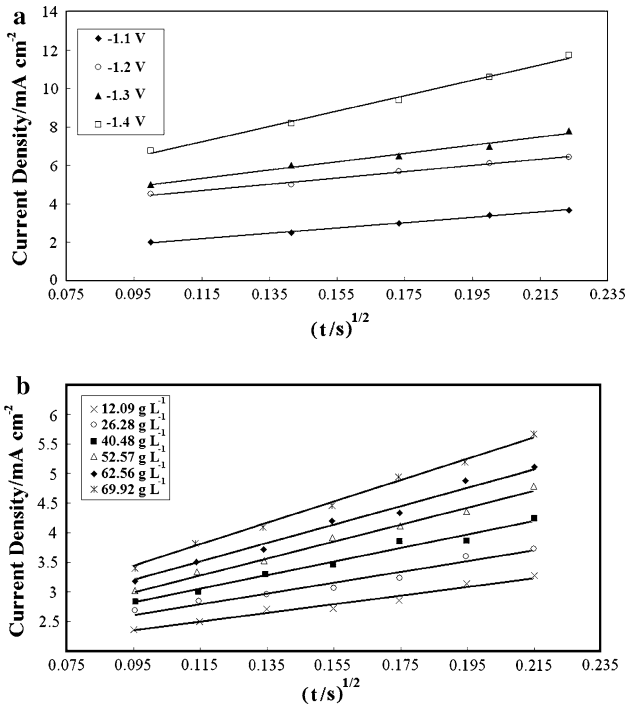

Fig. 6 Potentiostatic I–$t^{1/2}$ curves for deposition of the nickel; **a** in sol. 4, Ni^{2+} concentration = 57.52 g L^{-1} and **b** in sol. 4, Ni^{2+} concentration from 12.096 to 69.92 g L^{-1} for E = −1.25 V versus Ag/AgCl

overpotential. An increase of the slope with overpotential enhanced the nucleation sites.

The diffusion coefficients of nickel cations, which were calculated from the voltammograms, were used to obtain the number of nucleation sites on the surface. The number of nucleation sites (N_0) is obtained from the regression analysis of I versus $t^{1/2}$ curves as presented in Table 3a. Moreover, the slope of the lines in Fig. 6b was increased with increasing the nickel concentration as well as the number of nucleation sites (Table 3b).

Non-dimensional plots of I^2/I_m^2 versus t/t_m could be obtained from the I–t transients that the current I_m and the time t_m correspond to the maximum current. These plots with theoretical curves were derived from Sharifker equations for 3D instantaneous and progressive nucleation [17, 18], are shown in Fig. 7a for the electrodeposition of nickel using sol. 4 ($[Ni^{2+}]$ = 57.52 g L^{-1}). Nucleation mechanisms shifted toward the 3D instantaneous curve with increment of the overpotential. It is revealed from Fig. 7b that the nucleation mechanism was 3D instantaneous in sol. 4 for concentrated solutions.

The AFM was used to investigate the morphology of the deposits. The nickel films which were deposited, using sol. 4 with 0.2 M nickel concentration (Fig. 8a), consisted of regions with a typical fine spherical and uniform structure. The particle sizes varied between 50 and150 nm. Figure 8b illustrates the finer spherical nickel structure that was

Table 3 The number of nucleation sites (N_0) formed at various **a** overpotentials and **b** nickel concentrations

Potential (V)	N_0 ($\times 10^7$, cm^{-2})
−1.1	2.10
−1.2	2.21
−1.3	2.27
−1.4	2.31
$[Ni^{2+}]$ (g L^{-1})	N_0 ($\times 10^7$, cm^{-2})
12.09	2.10
26.28	2.15
40.48	2.18
52.57	2.21
62.56	2.25
69.96	2.28

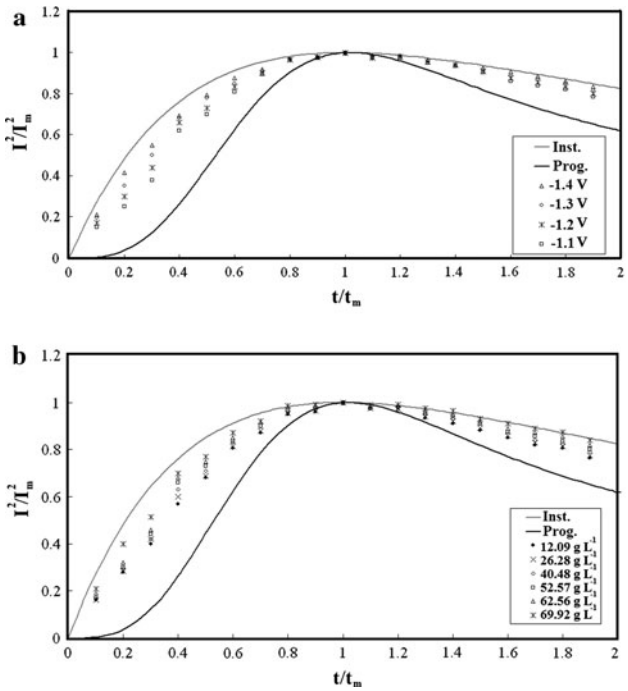

Fig. 7 I^2/I_m^2 versus t/t_m curves for deposition of the nickel, **a** in sol. 4, $[Ni^{2+}]$ = 57.52 g L^{-1} with potential ranges from −1.1 to −1.4 V versus Ag/AgCl and **b** in sol. 4, Ni^{2+} concentration from 12.09 to 69.92 g L^{-1} and E = −1.4 V versus Ag/AgCl

synthesized at −1.4 V in 69.92 g L^{-1} solution. It was revealed from electrochemical investigations that the higher concentration and higher overpotential increases the nucleation sites, and consequently, the finer structure will be obtained. In this case, the size of the spheres was about 20–50 nm. The nickel surface that was formed in a cumarine-free solution consists of sub-micron planes (Fig. 8c) with a 2D morphology.

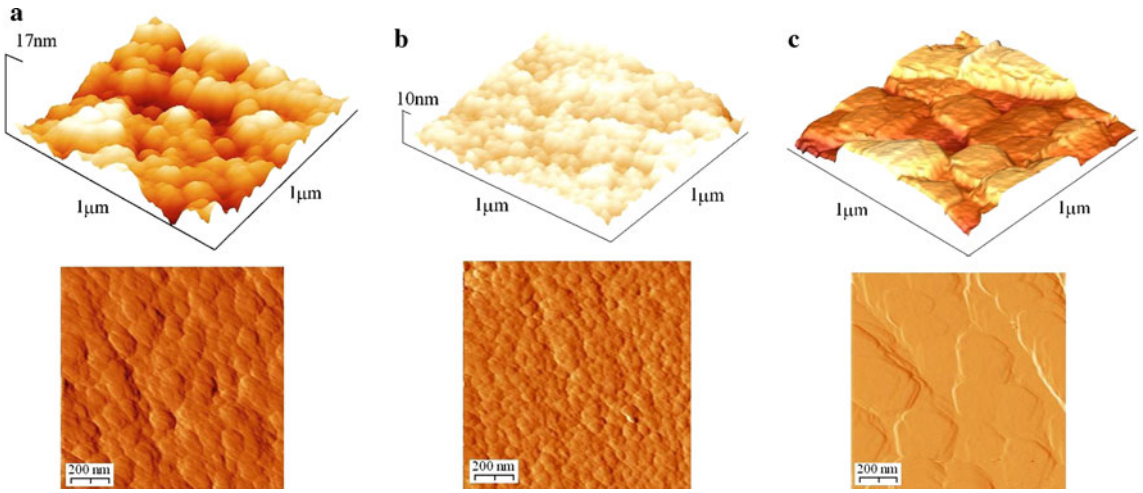

Fig. 8 AFM images of the Nickel electrodeposited in sulfate solution on the copper substrate, **a** in potential −1.2 V and $[Ni^{2+}] = 57.52$ g L^{-1} for deposition time 90 s, **b** electrodeposited Ni layer in potential −1.4 V and $[Ni^{2+}] = 69.92$ g L^{-1}, and **c** electrodeposited Ni layer in potential −1.2 V without Cumarine for deposition time 90 s

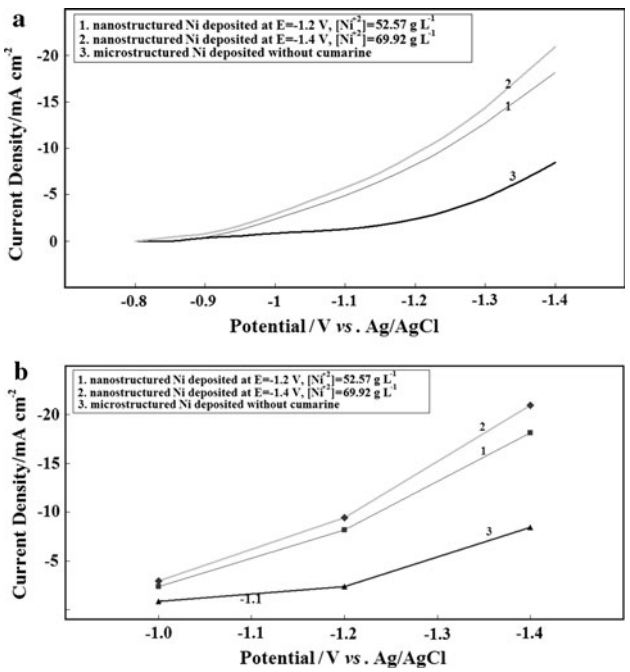

Fig. 9 **a** Polarization curves for hydrogen evolution in 39.99 g L^{-1} NaOH (Scan Rate: 5 mV s^{-1}) and **b** electrocatalytic activity of the nickel thin films

Electrocatalytic activities of the deposited thin films were evaluated for HER. The polarization curves in an alkaline solution (39.99 g L^{-1} NaOH) at room temperature are presented in Fig. 9a. The samples 1 and 2 that were electrodeposited using cumarine have lower overpotentials for HER (−0.9 V) than the sample 3 that was electrodeposited in a cumarine-free solution (−1.1 V). Also, the electrocatalytic activities of the films that are presented in Fig. 9b show that at overpotential of −1.2 V, the current density for sample 3 is −2.38 mA cm^{-2} while the current densities of the samples 1 and 2 are −8.19 and −9.45 mA cm^{-2}, respectively. These higher electrocatalytic activities of the samples 1 and 2 that have 3D morphologies might be due to larger active surface area.

4 Conclusion

The electrodeposition of nickel in the sulfate bath is a diffusion-controlled process with a typical nucleation process. The deposition in the solutions free of agents is charge-transfer controlled. The current transients show that with increasing the overpotential and cation concentration, the deposition is kinetic-controlled, as well. The nucleation sites are increased with increasing the overpotential and nickel concentration. Moreover, Sharifker's plots show the mix 3D nucleation. At higher overpotential and concentration, 3D instantaneous nucleation is more dominant. The AFM analysis showed that the growth was 3D whereas the deposited nickel film from cumarine-free electrolyte was 2D layer. The overpotential was reduced for HER and showed that the Ni nanostructure has higher electrocatalytic activity than the Ni microstructure.

References

1. Lindsay J (2004) Plat Surf Finish 107:1
2. Simon HK, Erb U, Aust KT, Gonzalez F, Palumbo G (2004) Plat Surf Finish 91:68
3. Palumbo G, Gonzalez F, Brennenstuhl AM, Erb U, Shmayda W, Lichtenberger PC (2004) Nanostruc Mater 9:737
4. Qu NS, Zhu D, Chan KC, Lei WN (2003) Surf Coat Tech 168:123

5. Karimpoor AA, Erb U, Aust KT, Palumbo G (2003) Scr Mater 49:651
6. Lu L, Tao NR, Wang LB, Ding BZ, Lu K (2001) J Appl Phys 89:6408
7. Nabirahni DMA, Tang PA, Leisner P (1996) Nanotechnology 7:134
8. Zimmerman AF, Palumbo G, Aust KT, Erb U (2002) Mater Sci Eng A 328:137
9. Lu L, Sui ML, Lu K (2000) Science 287:1463
10. Asaro RJ, Suresh S (2005) Acta Mater 53:3369
11. Lutfi N, Veziroglu TN (1991) Int J Hydrogen Energy 16:169
12. Greeley J, Jaramillo TF, Bonde J, Chorkendorff I, Nørskov JK (2006) Nat Mater 5:909
13. Divisek J, Malinowski P, Nergel J, Schmitz H (1988) Int J Hydrogen Energy 13:141
14. Divisek J, Schmitz H, Steffen B (1994) Electrochim Acta 39:1723
15. Miles MH, Kissel G, Lu PWT, Srinivasan S (1976) J Electrochem Soc 123:332
16. Heiland W, Gileadi E, Bockris JOM (1966) J Phys Chem 70:1207
17. Scharifker BR, Mostany J, Palomar-Pardave M, Gonzalez I (1999) J Electrochem Soc 146:1005
18. Scharifker BR, Hills G (1983) Electrochim Acta 28:879